ELSEVIER

Contents lists available at ScienceDirect

# CIRP Journal of Manufacturing Science and Technology

journal homepage: www.elsevier.com/locate/cirpj



# Brain-inspired computing for in-process melt pool characterization in additive manufacturing



Ruimin Chen <sup>a</sup>, Manbir Sodhi <sup>b</sup>, Mohsen Imani <sup>c</sup>, Mojtaba Khanzadeh <sup>d</sup>, Aref Yadollahi <sup>e</sup>, Farhad Imani <sup>a,\*</sup>, <sup>1</sup>

- <sup>a</sup> Department of Mechanical Engineering, University of Connecticut, Storrs, CT 06269, USA
- <sup>b</sup> Department of Mechanical, Industrial and Systems Engineering, University of Rhode Island, Kingston, RI 02881, USA
- <sup>c</sup> Department of Computer Science, University of California Irvine, Irvine, CA 92697, USA
- <sup>d</sup> Amazon.com, Tempe, AZ 85281, USA
- e Department of Mechanical and Civil Engineering, Purdue University Northwest, Hammond, IN 46323, USA

#### ARTICLE INFO

Available online 11 January 2023

Keywords: Additive manufacturing Quality monitoring Defect detection Cognitive computing

# ABSTRACT

Melt pool dynamics represent key information on defect creation in the laser powder bed fusion (LBPF) additive manufacturing process. In-situ sensing of the melt pool is now integrated with LPBF machines. Infrared cameras, optical emission spectroscopies, and photodiodes are utilized for real-time monitoring of thermal process signatures to mitigate defects for improving build quality. The detection of phenomena, including melt pool oscillations, laser modulation, plume formation, and spatter calls upon significant data acquisition rates, and photodiodes alone offer the necessary bandwidth. However, the high data velocity presents a significant computational challenge for training machine learning methods to supervise real-time monitoring. We propose a novel cognitive-based hyperdimensional computing (HDC) for one-pass learning of defects using measurements from photodiodes. We introduce several sampling for in-situ defect detection. Experimental results based on a real-world case build with overhang layers show that HDC is better at detecting defects than SVM (by 103.150%), KNN (by 104.545%), LDA (by 40.999%), and QDA (by 51.346%) while requires merely 0.273 ± 0.008 s for training. The proposed HDC is shown to be effective for fast single-pass training and eliminates the necessity of costly retraining for in-process monitoring in various additive manufacturing processes.

© 2022 CIRP.

# Introduction

Laser powder bed fusion (LPBF) is a family of additive manufacturing (AM) processes that leverage the high-power laser to melt the powder and form intricate 3D geometries layer by layer. Despite the potential to revolutionize manufacturing, fabricated LPBF builds currently suffer from quality issues, including anisotropic microstructure, lack-of-fusion, gas porosity, crack, inferior surface finish, recoater crash, and geometry distortion (e.g., overhang or failure in anchoring support) [1–3]. Defect incident in LPBF is associated with thermal dynamics such as cooling, melting, remelting, and solidification of powder, and can be categorized at two main levels [4–6]. The first is at the scan track level, where the rapid laser scan action

and persistent material melting at intense temperatures cause elevated cooling and heating cycles [7]. As a result, thermal history (i.e., nonuniform spatial-temporal temperature distributions) is created, which leads to residual stress and deformation of build [8]. The second level is related to the melt pool, where the stir-up of molten material is formed through the absorption of laser energy. Here, the morphology of melt pool varies relying on process factors together with material attributes [9]. The shape and temperature distribution of melt pools impact the microstructure properties, thereby leading to crack and porosity [10].

Since the thermal history and melt pool characteristics can significantly impact the quality of the LPBF build, in-situ measurements of thermal behavior are collected and analyzed to detect and mitigate various quality issues on the fly [11]. Popular sensing approaches at the scan-track level include tracking the layer temperature with infrared (IR) or near-infrared (NIR) thermal cameras and off- and co-axial pyrometers [12–14]. These sensors can

<sup>\*</sup> Corresponding author. E-mail address: farhad.imani@uconn.edu (F. Imani).

<sup>&</sup>lt;sup>1</sup> ORCID: 0000-0003-0837-9273.

capture emissions and rapid transient phenomena throughout the scanning task. The objective is to detect irregular cooling patterns by characterization of spatial-temporal data layerwisely.

The melt pool level characterization, on the other hand, is pertinent to properties of molten regions such as size, geometry intensity, and the radiation spectrum. Co-axial and off-axis mounted pyrometers (i.e., one or multiple photodiodes), co-axial video imaging, and optical emission spectroscopy are prevalent sensing techniques for measuring the melt pool radiation, size and shape, and emission spectrum [15,16].

While video imaging is useful for defect detection, phenomena such as melt pool oscillation and laser modulation often demand data measuring rates above 10 kHz [11,17]. In contrast, an inexpensive co-axial photodiode can provide a high-frequency 2D map of melt pool intensities by synchronizing with laser coordinates. As a single-point sensor, a photodiode has the temporal bandwidth to capture process signatures at the expense of spatial information. However, its high-speed data reading prevents monitoring nonstationary melt pool dynamics through powerful learning methods such as Bayesian inferences and convolutional neural networks (CNN), recurrent neural networks (RNN), and generative adversarial networks (GAN) [18]. As an example, consider an incipient defect that has to be addressed before the next pass to perform recoating and re-processing the defect with new powder. This window is of the order of 0.5-1 min, which is the major gap for the current quantitative models to capture and analyze data with high accuracy and robustness. In particular, neural networks require significant computational time and suffer from generalizability concerns due to the different geometries of parts in the LPBF process [19].

This study introduces a novel cognitive-based computing method to extract key features from the photodiode signal and detect incipient defects in the LPBF process in real time. The proposed hyperdimensional computing (HDC) is inspired by the fact that the human brain (i.e., cerebellum cortex lobes) recalls and differentiates basic and sophisticated concepts and notions with the help of hypervectors, not just singular values.

As shown in Fig. 1a), HDC represents human memory and develops more flexible operations supporting AM information association, memorization, and attention through mapping data in high-dimensional space. Fig. 1b) illustrates that each element of hypervector mimics the functionality of neurons to incorporate learning capability. Here, there exist a large number of high-dimension vectors that are approximately orthogonal. The orthogonality enables jointing hypervectors through common mathematics and restoring the knowledge with strong likelihood.

To further improve the learning capability, we integrate the notion of dynamical change (i.e., regeneration) in neurons (see Fig. 1c) [20]. In addition to the enhanced learnability of new information, the concept of regenerated brain cells augments the entire brain-inspired computing for refined adaptation and innovation. Therefore, HDC is able to capture important features within one iteration with limited data while providing robust learning results at the same time. In our experimental design, we first select the best encoding

dimension for the proposed HDC. Then, we compared various sampling strategies, namely no sampling, temporal sampling, spatial sampling, and spatial-temporal sampling to prevent the burden of high computational cost. Finally, we compare HDC with other machine learning methods regarding the capability to identify overhang issues from photodiode measurements in an LPBF build. The HDC provides cognitive functionalities such as (1) single-pass training that eliminates the necessity of costly retraining, (2) self-adaption to any problems with no or limited hyper-parameter selection, (3) faster convergence and few sample learning, and (4) robustness against manufacturing noise in photodiode measurements.

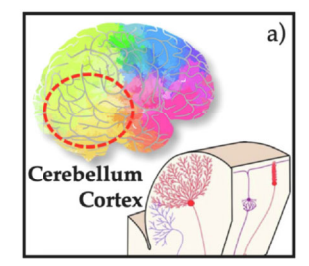
The remainder of this paper is organized as follows: Research background reviews state-of-the-art methods on in-situ thermal characterization and the cognitive computing. Methodology presents the proposed methodology. Experimental design and results of a parallel equipped build based on a real-world study are given in Experimental results. Conclusions concludes this research by featuring deficiencies of learning methods for melt pool characterization in AM and then discussing the future direction of the study.

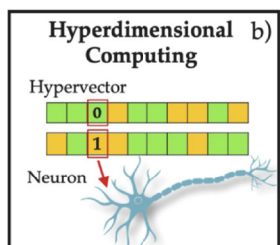
# Research background

Melt pool in-process monitoring

In-process monitoring requires high-rate measurements of emission and quick transient phenomena in the laser-based additive manufacturing process. While various sensors have been recently integrated to provide in-situ process signatures of the LPBF process, melt pool analysis has been at the center of many investigations. Comprehensive review articles recently published relating to current in-situ sensing trends for this popular AM process are [21–23].

Although optical and infrared cameras are conducive to capturing high-resolution data related to build quality [24–27], they are not as useful for capturing critical thermal spikes, a vital process signature. Photodiodes, which are single-point sensors, have a fast response rate and, as a result, can measure thermal spikes and are significantly cheaper [28]. Previous publications have focused on utilizing single-spot thermal reading for measuring radiation intensity with high-temporal resolution. For example, Craeghs et al. [29] designed a co-axial layout for monitoring LPBF melt pool using a visible camera and a near-infrared photodiode with a bandwidth of 400–900 nm. Yadroitsev et al. [30] installed two pyrometers to attain emissions in melt pool at various wavelengths in addition to a charge-coupled device camera for combining image radiance in transversal and longitudinal directions. Albert et al. [31] used a photodiode to explore the relationship between build density of Inconel 718 and thermal emission through measuring deviation in volume energy. Nadipalli et al. [32] and Bisht et al. [17] applied a similar approach for measurements of the melt pool that not only enables the collection of radiation signals, but also captures emissions from surrounding hot areas. Montazeri et al. [33] studied a coaxial photodiode that captures melt pool radiation and distinguishes the material composition for cross-contamination analysis.





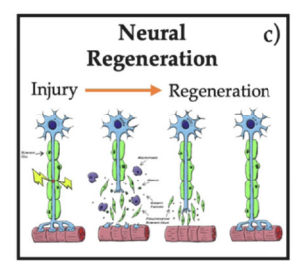


Fig. 1. Overview of the proposed hyperdimensional computing methodology.

Taherkhani et al. [34] designed an in-process sensing platform that leverages the intensity of radiated light from the melt pool to recognize porosity caused by lack of fusion.

Machine learning methods are also being integrated with LPBF processes to exploit in-situ photodiode data for defect detection [35]. For example, Okaro et al. [36] implemented a Gaussian mixture model for semi-supervised classification of photodiode signals of Inconel 718 component in LPBF. They reported a successful classification of void defects based on results with 49 tensile test bars. Jayasinghe et al. [37] developed a singular value decomposition method to obtain process signatures from photodiode data during the fabrication process. The K-means and Gaussian mixture models were applied to cluster the density of builds. They also utilized a Gaussian process regression method to estimate the density of AM builds in a supervised learning manner. Recently, Mitchell et al. [16] investigated a Gaussian filter model to detect outlier images and conditions that represent porosity in the build using pyrometry data.

Although previous works are conducive for melt pool characterization and monitoring using high-rate data, they are computationally expensive in online learning of high-velocity photodiodes data (i.e., Gaussian process and CNN), or they are dependent on arduous extraction of handcrafted features (e.g., PCA and K-mean). There is a need for more effective computing paradigms that can work directly with the high-speed data stream from single-point photodiodes and can perform real-time monitoring of defects in the LPBF process.

#### Brain-inspired hyperdimensional computing

Hyperdimensional computing is a type of cognitive paradigm in which data are processed in high-dimensional space to provide semantic reasoning and structured knowledge analysis. HDC encodes data and performs learning with similar precision compared to state-of-the-art while significantly reducing computational costs. The holographic representation of data in HDC makes the computing robust to communication errors. HDC entails encoding and arithmetic operations as two primary steps in computing. The encoding step, which maps raw data to the hypervectors, can have a length of 50,000 elements. There are various encoding methods in HDC, such as binary, ternary, dense, and sparse. In the second step, the basic operations, including nearest neighbor search and

rotations, are utilized to accelerate high-performance and cognitive learning in one-pass or multiple iterations [38].

HDC is inspired by investigations on the human brain that demonstrate handling basic psychological circumstances involves simultaneous operations of various detached nervous systems [39]. Motivated by this fact, HDC assigns a particular notion to activation pattern in several elements of hypervector [40]. Due to this encoding capability, the learning is immune to communication noise and can achieve a comparable accuracy with respect to the state-of-the-art methods within a few epochs and a limited number of training data [41].

Hence HDC has received considerable attention from different domains such as security, health diagnosis, DNA pattern matching, and robotics. For example, Imani et al. [42] introduced HDC for realizing agile security and privacy. Zou et al. [43] designed an HDC-based model called SpikeHD to tackle the problem with efficient and low-power computation on edge devices. Despite the promising capability of hyperdimensional computing for one-pass and real-time learning in various domains, the previous works have been limited to realizing in-process defect monitoring using high-temporal photodiode data in additive manufacturing processes.

# Methodology

In this paper, we explore hyperdimensional computing with high-velocity manufacturing data. As shown in Fig. 2, this research contains two main steps. Using laser power and photodiode measurements, we first explore the best encoding dimension of the proposed HDC. Then, several sampling strategies, namely no sampling, temporal sampling, spatial sampling, and spatial-temporal sampling, are studied to decrease the computational complexity of HDC. Finally, we compare the proposed computing with other machine learning methods to show a comparable performance for build monitoring in the LPBF process.

# Hyperdimensional computing operations

Hyperdimensional computing is a novel approach to information processing, where input data are encoded to higher dimensional vectors, which are then processed to represent information related to the domain of interest. Hyperdimensional computing uses a large

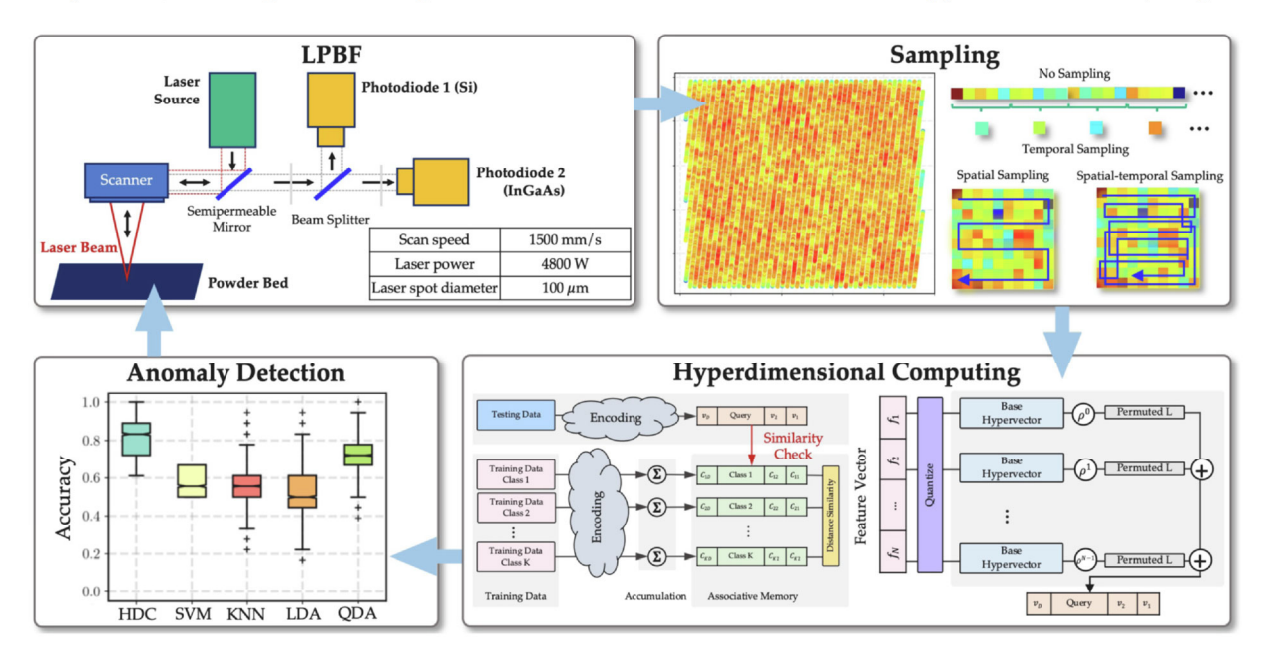


Fig. 2. Flowchart of proposed HDC to one-pass learning and detection of overhang defect using photodiode data.

number of approximately orthogonal hypervectors, each being thousands of dimensions in length [44]. These hypervectors are integrated into one high-dimensional vector through suitable arithmetic operators to retain the information of the initial space with high likelihood. The components of hypervectors are independent and identically distributed (i.i.d.) random variables, which leads to a holographic representation of long vectors [45]. Consequently, information is evenly distributed among the elements of each hypervector, which, in turn, prevents any piece of the hypervector from representing more features than others.

Consider  $\overrightarrow{V_1}$ ,  $\overrightarrow{V_2}$  as two created hypervectors  $(\overrightarrow{V} \in \{-1, +1\}^D)$  and  $\Delta(\overrightarrow{V_1}, \overrightarrow{V_2}) \approx 0$ . In HDC, the following operations are performed on  $(\overrightarrow{V_1}, \overrightarrow{V_2})$ :

- **Binding** (\*) of the two hypervectors  $\overrightarrow{\mathscr{V}_1}$  and  $\overrightarrow{\mathscr{V}_2}$  is performed through element-wise multiplication and is expressed as  $\overrightarrow{\mathscr{V}_1} * \overrightarrow{\mathscr{V}_2}$ . This operation creates an additional hypervector that is different from parent vectors i.e.,  $\Delta(\overrightarrow{\mathscr{V}_1} * \overrightarrow{\mathscr{V}_2}, \overrightarrow{\mathscr{V}_1}) \approx 0$ . Hence this binding operation associates two hypervectors, which is crucial for cognitive operations such as mapping and association.
- **Bundling (+)** is the addition of hypervectors in an element-wise manner and is expressed as  $\overrightarrow{\mathscr{V}_1} + \overrightarrow{\mathscr{V}_2}$ . The bundling operation provides a memorization capability, maintaining the information of multiple data. The bundled hypervector conserves similarity to the parent hypervectors i.e.,  $\Delta(\overrightarrow{\mathscr{V}_1} + \overrightarrow{\mathscr{V}_2}, \overrightarrow{\mathscr{V}_1}) >> 0$ . Thus, the bundling function is appropriate for set representation.
- **Permutation**  $(\rho)$   $\rho^n(\overrightarrow{\mathcal{V}})$ , shifts elements of  $\overrightarrow{\mathcal{V}}$  through an n-bit (s) permutation. This operation generates a reversible and a near-orthogonal hypervector, i.e.,  $\Delta(\rho^n(\overrightarrow{\mathcal{V}}), \overrightarrow{\mathcal{V}}) \simeq 0$  when  $n \neq 0$  and  $\rho^{-n}(\rho^n(\overrightarrow{\mathcal{V}})) = \overrightarrow{\mathcal{V}}$ . As a result, the orders and sequences can be protected.
- **Reasoning** is performed by using the correlation between hypervectors. The cosine similarity is defined via  $\Delta(\overrightarrow{\mathcal{V}_1}, \overrightarrow{\mathcal{V}_2})$ .

#### Hyperdimensional computing basics

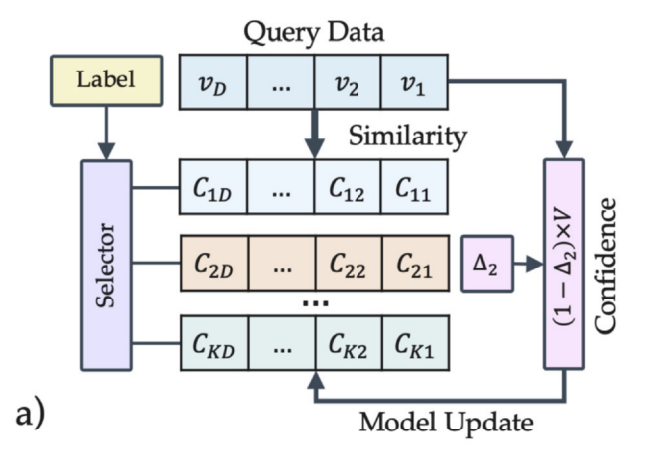
HDC comprises of following steps: encoding, single-pass training, inference, and retraining. Hypervectors, as the fundamental piece of computation in HDC, are created by encoding raw signals. During training, HDC superimposes encoded signal values to create a composite representation of a phenomenon of interest known as a "class hypervector". Then, the nearest neighbor search identifies an appropriate class for the encoded query in inference.

#### Encoding

We first utilize an encoding algorithm to transform all data into a high-dimensional space. HDC is designed to work with various encoding methods in line with the fact that data are separated in high-dimensional space if they are a long way apart in the normal space [46]. Therefore, two encoded hypervectors will be orthogonal (i.e., the cross product of two vectors will be zero) if the two corresponding original data points are entirely different from each other. We denote the  $\overrightarrow{\mathbb{F}} = \{f_1, f_2, ....f_N\}$ , as a vector with N features that is mapped to a hypervector using an encoding function. The hypervector is represented as  $\overrightarrow{\mathbb{F}} = \{v_1, v_2, ..., v_D\}$  with D dimensions (D > N). The encoding procedure can be shown as

$$\overrightarrow{\mathscr{V}} = \sum_{k=1}^{N} |f_k|_{\in \mathscr{F}} \cdot \mathscr{B}_k^{\overrightarrow{k}} \tag{1}$$

where  $\overrightarrow{M}_k$  represents orthogonal hypervectors with binary base to retain the time-space properties of input features, and  $D \le 50k$ .



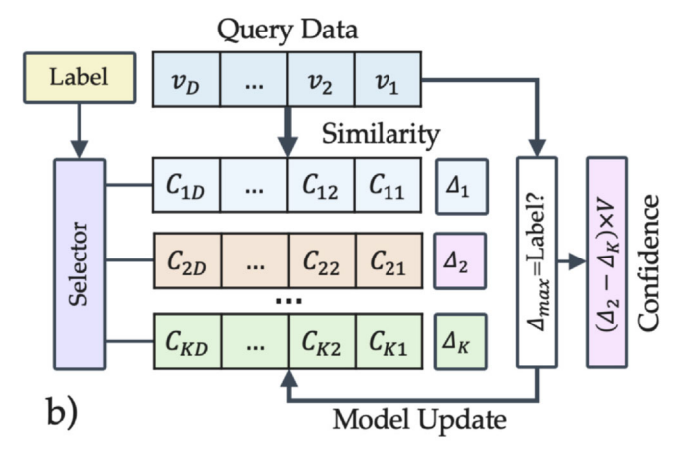


Fig. 3. a) single-pass training in hyperdimensional computing; and b) HDC with adaptive iterative training.

Therefore, we have  $\overrightarrow{\mathscr{D}_k} \in \{-1, 1\}^D$ , and the cosine similarity  $\Delta(\overrightarrow{\mathscr{D}_{k_1}}, \overrightarrow{\mathscr{D}_{k_2}}) \simeq 0$ .

#### **Training**

Single-pass training aims to discover the global attributes in the data. HDC leverages binding or bundling operations to construct a class hypervector (i.e., in the classification task) by linearly combining hypervectors in each class. For the classification task with K classes  $\mathscr{M} = \{\overrightarrow{e_1}, \overrightarrow{e_2}, ... \overrightarrow{e_K}\}$  and  $\mathscr{L}$  inputs with label I, the class hypervector  $\overrightarrow{e_l}$  is denoted as  $\overrightarrow{e_l} = \sum_i^{\mathscr{L}} \overrightarrow{\mathcal{V}}_i^l$ . However, the hypervector generation method described above

However, the hypervector generation method described above might result in misclassification due to the saturation of class hypervectors for prevailing patterns. Hence we propose an adaptive training model that determines and removes widespread attributes to prevent class hypervector saturation. Our new model combines each encoded data to class hypervectors according to the amount of additional information each pattern provides.

Fig. 3a) illustrates HDC procedure for adaptive training. For a new training data  $\overrightarrow{V}$ , HDC estimates the closeness to entire class hypervectors using the cosine similarity function, i.e.,  $\Delta(\overrightarrow{V}, \overrightarrow{V})$ . According to the results of the cosine similarity function,  $\Delta$ , the HDC is updated. For instance, we update the model through the following equation, if data point l is linked to class l':

$$\vec{\mathcal{C}_{l}} \leftarrow \vec{\mathcal{C}_{l}} + \eta(1 - \Delta_{l}) \vec{\mathcal{V}} 
\vec{\mathcal{C}_{l'}} \leftarrow \vec{\mathcal{C}_{l'}} - \eta(1 - \Delta_{l'}) \vec{\mathcal{V}}$$
(2)

where  $\eta$  represents the learning rate. When a query data holds different patterns than existing ones in HDC, (Eq. (2)) updates to a higher value (1 –  $\Delta_l \simeq 1$ ). Otherwise, we only add a lower value of the query to the class hypervector (1 –  $\Delta_l \simeq 0$ ).

#### Inference

This step is designed to calculate the correlation between class hypervector and input testing data. First, testing data is encoded into a hypervector  $\overrightarrow{\mathscr{V}}$ . Since there might be multiple classes where testing data can manifest high similarity, the query hypervector is appointed to a class with maximum correlation. In the last step, HDC is retrained by removing the mispredicted queries from pertinent classes and assigning them to the proper class.

#### Retraining

Fig. 3b) shows the adaptive learning capability of HDC. Similar to the initial training, adaptive learning offers more weight and possibility to unseen patterns to describe the trained model. Particularly, this procedure checks if HDC yields the correct label of an encoded query  $\overrightarrow{V}$ . If the correct label l is mispredicted by l', we leverage  $\Delta_l = \Delta(\overrightarrow{V}, \overrightarrow{Q_l})$  and  $\Delta_{l'} = \Delta(\overrightarrow{V}, \overrightarrow{Q_l})$  to compute the correlation of query hypervector with mispredicted and correct classes using Eq. (2). This step guarantees HDC is adjusted according to the amount of miss-classification in the training data point. In addition, the distinct factors for mispredicted and correct labels enable the proposed framework to update each hypervector of each class independently.

#### **Experimental results**

In this section, we first discuss the LPBF experiment performed and the dataset utilized in this research. Then, we describe how to obtain the best encoding dimension for the dataset when learning with the proposed HDC. Considerations underlying the selection of the best sampling method to reduce the calculation burden are then explained. Finally, HDC is benchmarked with other state-of-the-art machine learning methods.

# Experiment and dataset

We evaluate and validate the proposed methodology through an open-source dataset run by Politecnico di Milano [47] and Trumpf [48]. The specimen is fabricated with a Trumpf TruPrint 5000 multilaser LPBF production system [49]. First, the CAD design is converted to a stereolithography (STL) file prior to the printing process and is approximated and sliced to encompass the layerwise information of printing geometry [50]. The printing procedure is captured with two photodiodes during the fabrication process (See Fig. 2). This research leverages data collected by indium gallium arsenide (InGaAs) photodiode, a spatially-integrated sensor that is co-axially mounted in the chamber of the machine. Here, photodiode 2 deals with the melt pool radiation in the range of near or short infrared. The melt pool's side and top views along the laser path are illustrated in Fig. 4, and are the region the laser liquefies the powder. This is the main focus in any laser-based additive manufacturing process since the beammaterial interplay governs process dynamics and is responsible for the quality of the final build.

The build printed in the experiment is a parallelepiped of size  $10 \times 10 \times 25$  mm. Fig. 5 is a graphical representation of the fabricated part with bulk layers, unexposed layers, and overhang layers. The build is fabricated vertically along the z-direction with AlSi10Mg powder, a laser spot diameter of  $100 \, \mu m$ , a laser power of  $480 \, W$ , and a scan speed of  $1500 \, mm/s$ . As shown in Fig. 5, the dataset does not include the information related to the bottom layers as the process was not in regime conditions at the base areas. The bulk layers are

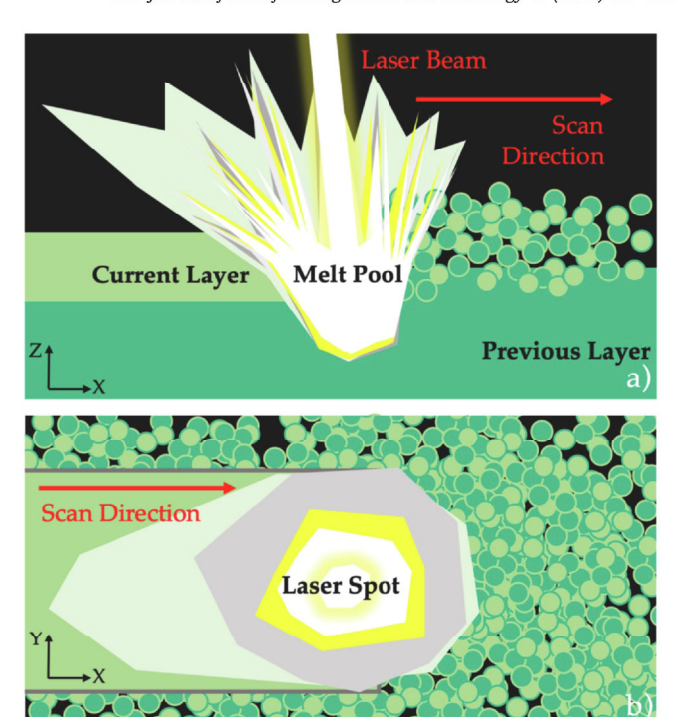


Fig. 4. Views of laser scan direction and the melt pool: a) top view, and b) side view.

fully printed layers without any gaps and hence are considered as incontrol data in this study. The unexposed layers correspond to the intentionally blocked areas designed to force heat exchange anomalies for overhang layers. The quantity of concealed layers inside each undisclosed cube elevated from 1 to 10 along the z-direction. Overhang layers are out-of-control layers in red. The overhang problem in LPBF often occurs when printing on loose powder instead of solid bulk materials. In the experiment, unexposed blocks (See Fig. 5) are designed to be printed with the number of unexposed layers that increases along the build direction. Therefore, the first layer (at the top) of the unexposed block has a large overhanging area with loose powder underneath. The heat exchange in this overhanging layer, also in a few of the layers that follow it, is altered by the fact that the loose powder has substantially smaller conductivity than the bulk material. Based on the observation from the post-process X-ray computed tomography, the first three layers following an unexposed block have overhang problem, which is considered to be out-of-control in the following analysis [49].

The dataset represents nine variables - the X and Y positions, NominalPower, NominalSpeed, NominalSpotDiameter, LaserPowerCurrent, SignalInGaAs, IDbulkLayer, and IDoocLayer. The X and Y coordinates are measured at the center of the photodiode's field of view. The NominalPower, NominalSpeed, and NominalSpotDiameter are nominal machine parameters specified for the build. LaserPowerCurrent and SignalInGaAs vary point-to-point and are the two variables focused on in this research. Note that the initial sampling rate of InGaAs is 100 kHz; however, it is down-sampled to achieve a single data point every 30 µm in the direction of the laser path. The direction of scan changes in every layer as is commonly implemented in LPBF. In total, 7 different scanning patterns are created as shown in Fig. 6. IDbulkLayer and IDoocLayer are two indicator variables related to the quality condition (i.e., in-control or out-of-control) of each layer. Detailed information related to each of the variables is shown in Table 1.

We select signals from SignalInGaAs of two layers, a control layer (i.e., layer 45) and an out-of-control layer (i.e., layer 61), for visualization. Fig. 7 shows the heatmap related to melt pool temperature

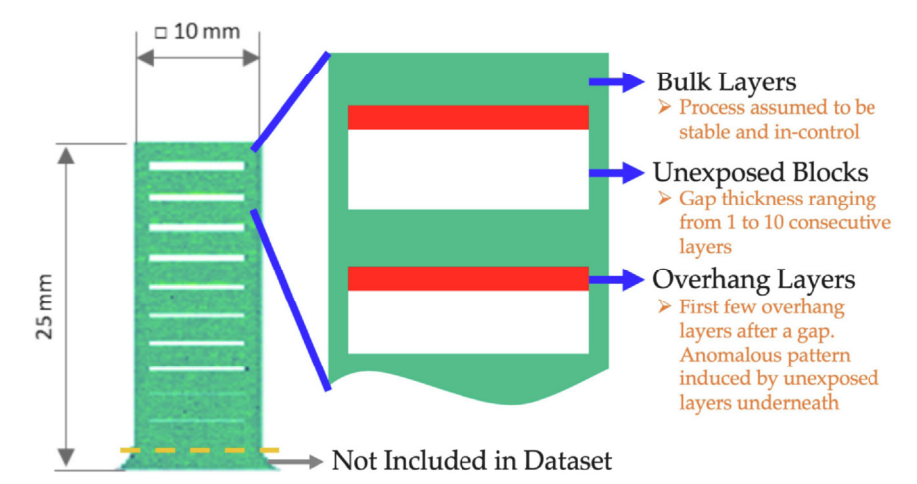


Fig. 5. Summary of the fabricated build with bulk layers, unexpected blocks, and overhang layers. The bulk layers in green are fully printed without any gaps and are considered in control. The overhang layers in red are out-of-control and are introduced by the exposed blocks in white. The first three layers above unexposed blocks are considered overhang layers. The data relating to the unexposed blocks are excluded from this research.

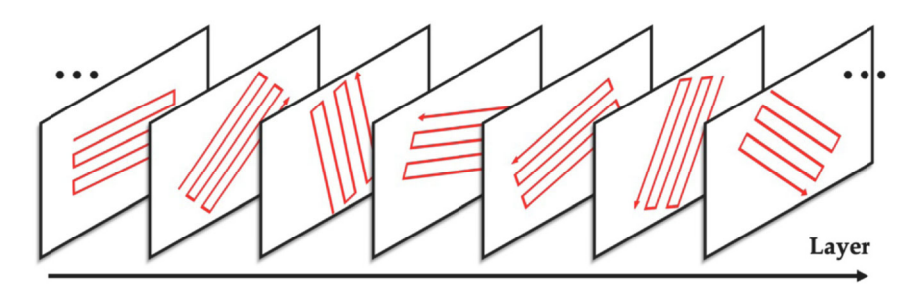


Fig. 6. Illustration of various scan paths in consecutive layers.

**Table 1**Detailed information of variables contained in the dataset.

Data	Description
X	Laser position in X direction (mm).
Y	Laser position in Y direction (mm).
NominalPower	Standard power (W).
NominalSpeed	Standard scan speed (mm/s).
NominalSpotDiameter	Standard diameter of laser point (in $\mu$ m).
LaserPowerCurrent	Captured laser power (W).
SignalInGaAs	Measuring obtained through the photodiode, proxy of the melt pool temperature.
IDbulkLayer	Binary variable, where 1 represents the bulk layers, and 0 indicates the layers related to unexposed blocks. The bulk layers are considered incontrol in this study.
IDoocLayer	Variable indicate the overhang layers. The value of this integer variable ranges from 0 to 9, where 0 indicates the first overhang layers introduced by the first unexposed block at the bottom, and 9 represents the last overhang layer related to the block at the top.

distribution across the layer. The dark solid lines indicate the travel path of the laser beam. As a common practice in LPBF, the direction of the laser path was changed in every layer. The blue arrow represents the starting point of the laser. In both layers, the laser travels in a chevron pattern to form a solid layer.

#### Selection of encoding dimension

As mentioned in *Methodology*, HDC first encodes the data into a hot vector. Fig. 8 illustrates the accuracy of HDC when the encoding dimension increases. Note that accuracy is calculated as

$$ACC = (TN + TP)/(TN + TP + FP + FN)$$
(3)

where TN, TP, FP, and FN, represent true negative, true positive, false positive, and false negative in the confusion matrix, respectively. It is worth mentioning that the ACC counts the number of correctly predicted data points (i.e., TN and TP) and divides them by the total

number of data points. When the embedding dimension is small, the accuracy of the proposed algorithm is small. This shows that the encoder cannot capture enough information to characterize the melt pool property. The accuracy converges when D=10,000. Simultaneously, the computational cost utilized for the algorithm increases linearly as the dimension gains. We keep the encoding dimension to 10,000 for the next steps.

#### Selection of sampling method

Next, we explore the effect of data sampling strategies on the performance of HDC. The detailed information on various sampling strategies is as follows:

 No Sampling: Utilizing the original data, we concatenate the two signals, LaserPowerCurrent and SignalInGaAs, of each layer to a long vector for the proposed HDC.

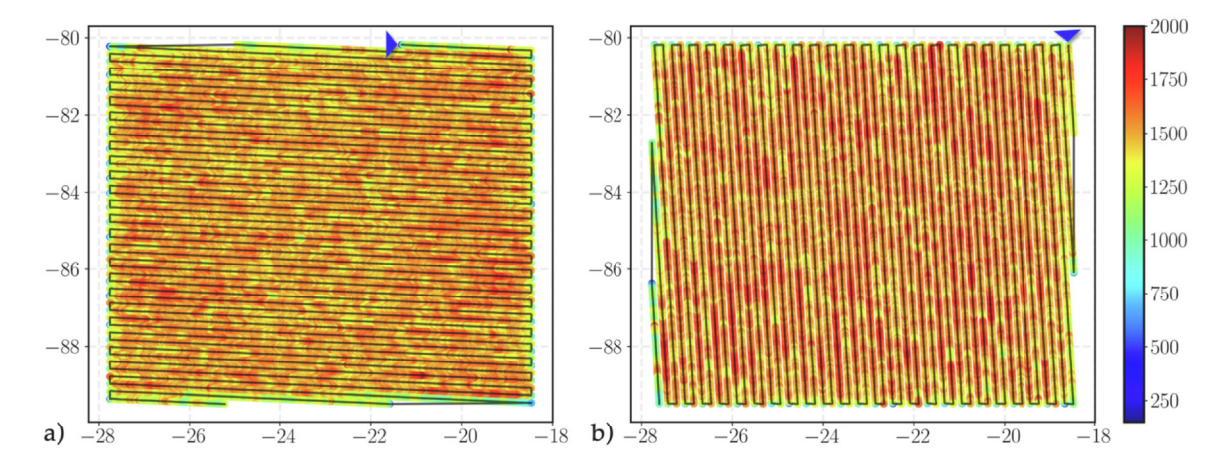


**Fig. 7.** Heatmaps of melt pool temperatures for a) layer 45, an in-control layer, and b) layer 61, an out-of-control layer. The blue arrow indicates the travel direction of the laser. Dark solid lines show the travel path of the laser beam.

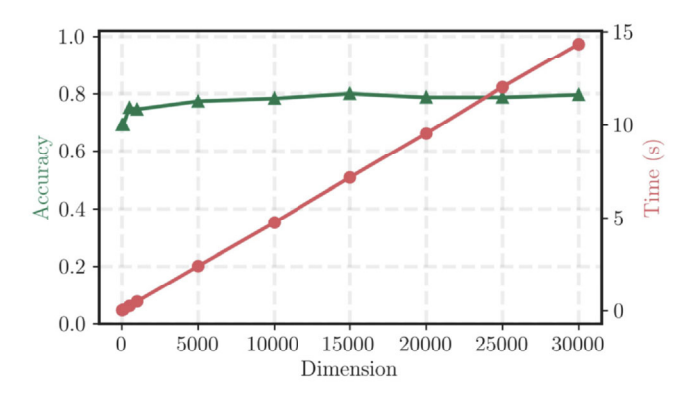


**Fig. 8.** Model performance (in green) and computational complexity (in red) under various HDC embedding dimensions.

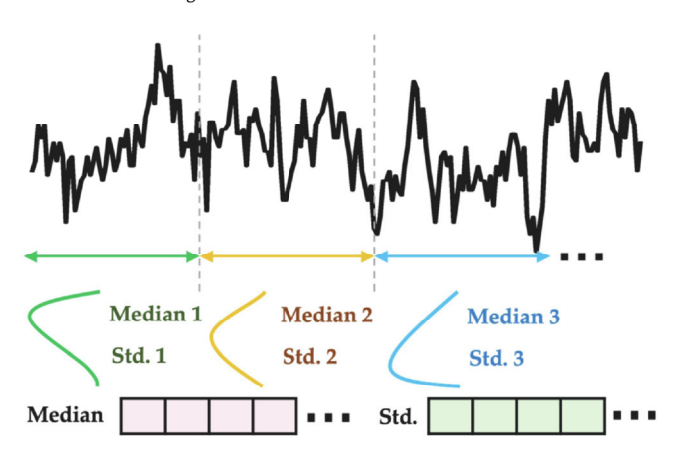


**Fig. 9.** Illustration of temporal sampling of a signal. Median and standard deviation of distribution in each window are extracted and concatenated for further analysis.

• **Temporal Sampling:** We sample the original data in a temporal manner. Fig. 9 demonstrates the idea of temporal sampling. For each layer (e.g., LaserPowerCurrent, SignallnGaAs), we sample from signal data with a window size of ω. Generally, the choice of window sizes (i.e., ω) depends on the data acquisition rate, the dimensionality of input data (number of channels), the dynamics of captured data, and the complexity of learning task (e.g., number of classes in classification). Fig. 10 shows the accuracy and the computational complexity of the proposed model regarding various window sizes ω. We varied the window size from

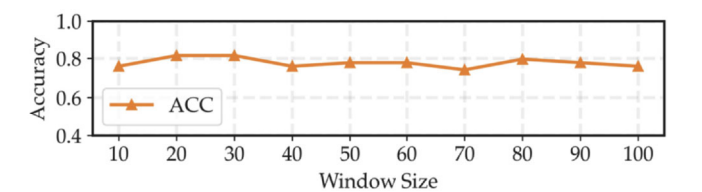
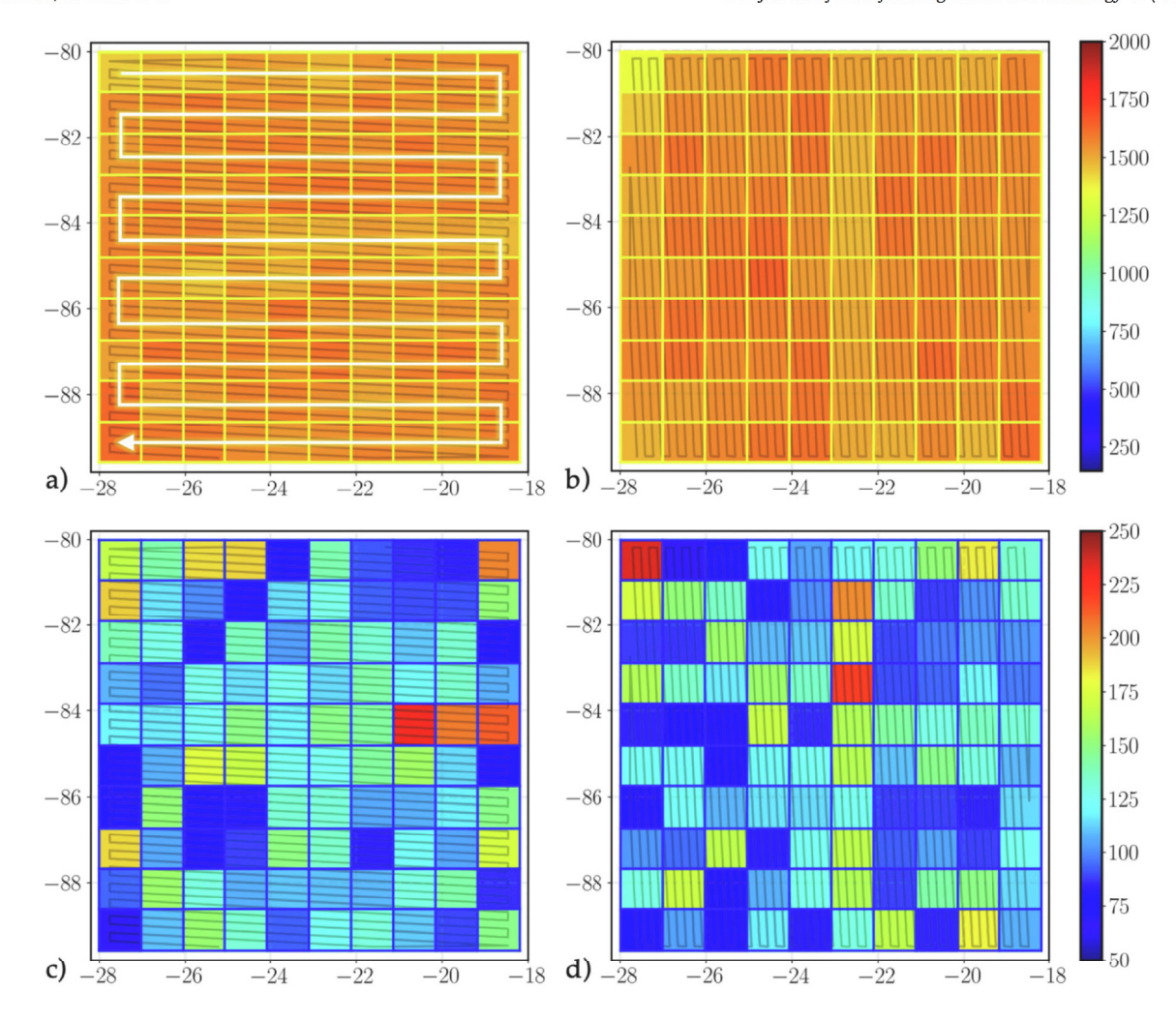


Fig. 10. Model performance under various window sizes.

10 to 100 with a step size of 10. Results show that the variation in window size has little impact on the model performance. As the next step,  $\omega$  = 20 was selected for further analysis as it provides the best performance in the comparison. Distributions between data in each window might be different. For example, the distribution in the first window (i.e., in green color) is negatively skewed, while the distribution in the third window (i.e., in blue color) is skewed positively. In comparison with the mean value, the median of the distribution is less sensitive to extreme values as they are common in real-world datasets. Consequently, we evaluate the median and deviation of each window and concatenate them into a long vector.

- **Spatial Sampling:** In the dataset, the range of X coordinates is (- 18, 28), and the range of Y coordinates is (- 80, 90). We mask a 10-by-10 grid for each layer to perform spatial sampling. As shown in Fig. 11, the white arrow in (a) indicates the sequence of concatenation in each layer. For each layer, we start sampling at the top left block and sample in the same sequence. After locating the signal in each block, we export the median and standard deviation of each block. Fig. 11 shows heatmaps of median and standard deviation of melt pool temperatures of two layers, layer 45 (i.e., an in-control layer) and layer 61 (i.e., an out-of-control layer), respectively. Therefore, each layer is downsampled to a vector of size 200.
- Spatial-temporal Sampling: In the actual fabrication process, the laser path does not follow the spatial masks. For example, in layer 45, the laser path travels back and forth multiple times in a block. Therefore, in spatial-temporal sampling, we consider not only the spatial relationship among data, but also the temporal information. As such, we extract the standard deviation and median of the distribution each time the laser stays within a block. The size of each vector is longer than the vector when performing spatial sampling.

In total, we have 297 bulk layers and 27 layers with overhang quality issues in our dataset. To prevent the overfitting of the



**Fig. 11.** Examples of median and variances extracted for spatial sampling. a) Median extracted from layer 45, an in-control layer; b) Median extracted from layer 61, an out-of-control layer; c) Standard deviation extracted from layer 45, an in-control layer; and d) Standard deviation extracted from layer 61, an out-of-control layer. Dark solid lines show the travel path of the laser beam. The white arrow in a) shows the concatenation detail of spatial sampling.

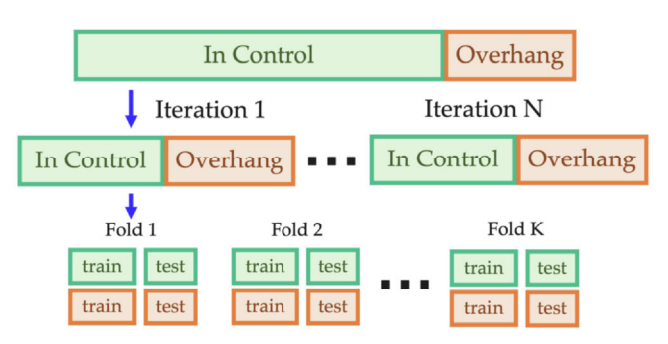


Fig. 12. An illustration of the K-fold experiment involved in the experiment.

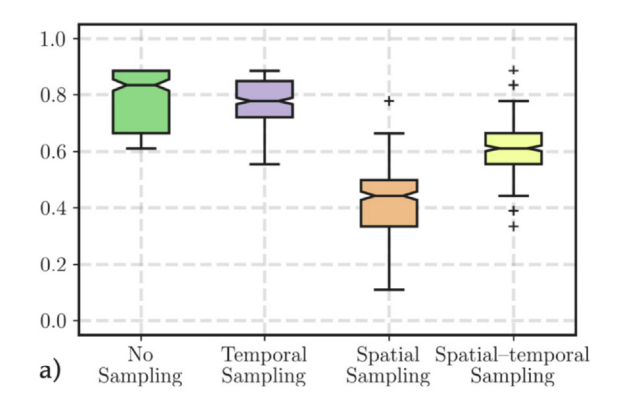
learning process, K-fold cross validation (i.e., K = 5 in our case) is implemented to assess the performance of HDC, without being concerned about the overfitting problem. As shown in Fig. 12, we randomly select 27 bulk layers from the in-control group and train them together with the out-of-control layers to prevent introducing bias. Therefore, we have 54 data points in each iteration, including the same number of in-control and out-of-control layers. We also keep the dataset small due to the key capability of HDC to work with a limited amount of training data. In total, we perform our experiment for 100 iterations, with 70% training and 30% testing. We calculate the testing accuracy as well as the F-score for performance

comparison. The accuracy is represented in *Methodology*, and F-score is calculated by the following equations:

$$F - score = \frac{TP}{TP + \frac{1}{2}(FP + FN)} \tag{4}$$

Again, TP, FP, and FN represent true positive, false positive, and false negative in the confusion matrix, respectively. Fig. 13 shows the performance comparison between different proposed sampling methodologies.

Here, all sampling methodologies impact the model performance and the best performance is achieved when we do not perform sampling. When only considering the temporal information, the impact is less than adding the spatial information. The accuracy and the F-score significantly decrease when performing the spatial sampling. This is because spatial sampling is limited to incorporating the travel path of the LPBF laser. When sampling the data both with spatial-temporal information, the performance of the HDC is slightly better than only sampling with the spatial information. In addition, the variance of the accuracy and F-score is smaller when performing the temporal sampling. This indicates that this sampling methodology is more robust in comparison with the other two. From the result in Fig. 13, the temporal relationship between data contains more meaningful knowledge related to process characteristics compared to the spatial statistics.



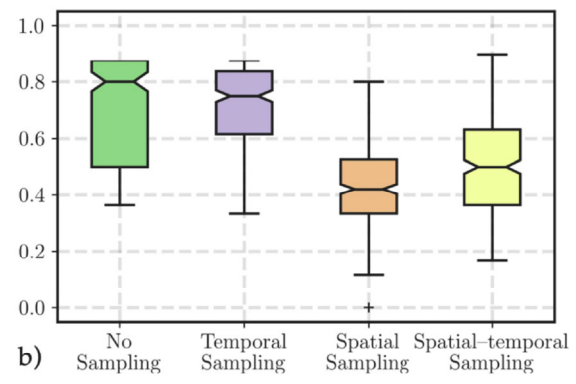


Fig. 13. Comparison among various sampling methodologies regarding a) Accuracy; and b) F-score.

**Table 2**Training time of the proposed HDC under various sampling methodologies.

Sampling Method	Time (s)
No Sampling Temporal Sampling	4.839 ± 0.067 0.273 ± 0.008
Spatial Sampling Spatial-temporal Sampling	0.081 ± 0.005 0.078 ± 0.008

**Table 3** Parameter setting for benchmark methods.

Benchmark Method	Parameters
Support Vector Machine	Kernel function: Radial basis function
K Nearest Neighbor	Number of neighbors: 2, Distance
	Metric: Euclidean
Linear Discriminant Analysis	Solver: Singular value decomposition
Quadratic Discriminant Analysis	Solver: Singular value decomposition

The results show that HDC is not only robust but also efficient. Here, we also report the time utilized for model training under different sampling methodologies in Table 2. Although our training process only takes, on average, 4.839 s even without sampling, the temporal sampling shortens the training time by 94.36%. It can also be noted that temporal sampling requires slightly more training time than spatial sampling and spatial-temporal sampling. Therefore, considering both the model performance (i.e., Accuracy and F-score) and the computational complexity (i.e., computational time), we choose temporal sampling to compare our proposed methodology with common machine learning methods.

#### HDC performance

Finally, we compare the HDC with four other machine learning methods, namely support vector machine (SVM) [51], K-nearest

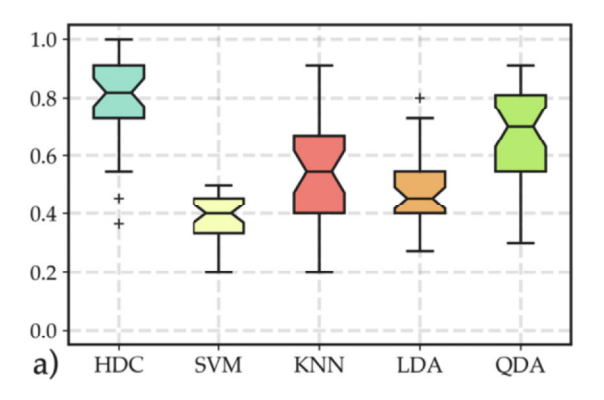


**Table 4**Accuracy and F-score based on test results from the proposed HDC and the benchmark methods support vector machine, k nearest neighbor, linear discriminant analysis, and quadratic discriminant analysis.

Methodology	Accuracy	F-score
HDC	0.805 ± 0.163	0.745 ± 0.214
Support Vector Machine	$0.385 \pm 0.077$	$0.324 \pm 0.286$
K Nearest Neighbor	$0.540 \pm 0.183$	$0.399 \pm 0.296$
Linear Discriminant Analysis	$0.489 \pm 0.127$	$0.501 \pm 0.174$
Quadratic Discriminant Analysis	0.668 ± 0.153	0.710 ± 0.148

neighbor (KNN) [52], linear discriminant analysis (LDA) [53], and quadratic discriminant analysis (QDA) [54], respectively. All benchmark methods are implemented through Python Sckit-learn library. A detailed summary of the parameters of all benchmark methods is presented in Table 3. Note that the number of neighbors K in the KNN model is optimized based on the best testing accuracy (i.e., selected from range [1,15]).

Here, the testing accuracy and F-scores for all methods are calculated based on their corresponding results. Similar to the previous experiment, the TP, FP, FN, and TN are first calculated by comparing prediction results with ground truth. Then, the accuracy and F-score are calculated according to Eqs. (3) and (4). As shown in Fig. 14, the proposed HDC outperforms other methods with regard to both testing accuracy and F-scores. Specifically, the HDC provides a testing accuracy that is 103.150% better than SVM, 104.545% better than KNN, 40.999% better than LDA, and 51.346% better than QDA, respectively. Further, the exact number of testing accuracy as well as F-score are summarized in Table 4. Therefore, the experimental result shows that our proposed HDC offers superior performance to other state-of-the-art algorithms and shows strong potential in understanding small AM datasets.

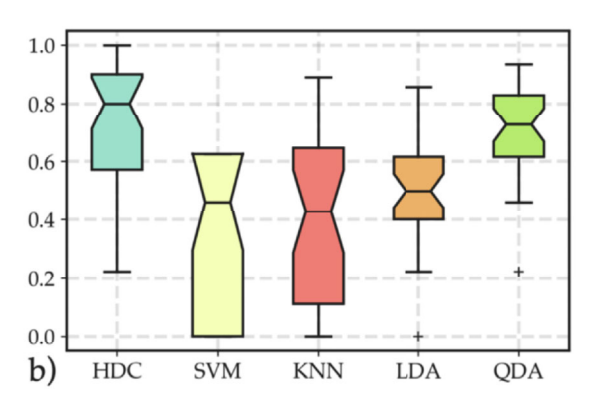


Fig. 14. Performance comparison between the proposed HDC and other methods regarding a) Accuracy and b) F-score.

#### **Conclusions**

Despite the effectiveness of in-situ photodiode sensing in capturing melt pool dynamics of laser powder bed fusion additive manufacturing, the high-temporal bandwidth is a challenge for online defect detection using current learning methods. We proposed a novel hyperdimensional computing (HDC) paradigm to analyze the high-velocity laser powder bed fusion additive manufacturing data. First, the optimal encoding dimension of the proposed HDC was investigated to enable a parsimonious representation of data. Second, various sampling strategies, namely no, temporal, spatial, and spatial-temporal, are introduced to realize authentic online learning via the proposed methodology. Third, the proposed HDC has been compared with widely used learning methods through accuracy and F-score criteria. Experimental results show that the proposed HDC leads to more robust results in the real-time detection of overhang defects in comparison with other machine learning methods. Furthermore, based on our observation, the temporal information of the signal from photodiode plays a more critical role than the spatial information from the part design. Future works include novel encoding methodologies that consider spatial information for high-dimensional data.

# **Declaration of Competing Interest**

The authors declare that they have no known competing financial interests or personal relationships that could have appeared to influence the work reported in this paper.

#### Acknowledgments

This work was partially supported by Semiconductor Research Corporation (SRC) [Task No. 2988.001], Department of the Navy, Office of Naval Research, [grant # N00014-21-1-2225], National Science Foundation (NSF) [grant # 2127780], and a generous gift from Cisco.

#### References

- [1] Sames, W.J., List, F., Pannala, S., Dehoff, R.R., Babu, S.S., 2016, The metallurgy and processing science of metal additive manufacturing. International Materials Reviews, 61:315–360.
- [2] Imani, F., Khanzadeh, M., 2021. Image-guided multi-response modeling and characterization of design defects in metal additive manufacturing. In: Proceedings of the ASME International Mechanical Engineering Congress and Exposition, Volume 85567, American Society of Mechanical Engineers, V02BT02A046.
- [3] Chen, R., Reutzel, E.W., Khanzadeh, M., Imani, F., 2022, Heterogeneous quality characterization and modeling of thin wall structure in additive manufacturing. Additive Manufacturing Letters:100042.
- [4] Grasso, M.L.G., Remani, A., Dickins, A., Colosimo, B., Leach, R.K., 2021, In-situ measurement and monitoring methods for metal powder bed fusion-an updated review. Measurement Science and Technology, 32.
- [5] Khairallah, S.A., Anderson, A.T., Rubenchik, A., King, W.E., 2016, Laser powder-bed fusion additive manufacturing: Physics of complex melt flow and formation mechanisms of pores, spatter, and denudation zones. Acta Materialia, 108:36–45.
- [6] Zhao, X., Imandoust, A., Khanzadeh, M., Imani, F., Bian, L., 2021. Automated anomaly detection of laser-based additive manufacturing using melt pool sparse representation and unsupervised learning. In: Proceedings of the International Solid Freeform Fabrication Symposium, University of Texas at Austin.
- [7] Smoqi, Z., Gaikwad, A., Bevans, B., Kobir, M.H., Craig, J., Abul-Haj, A., Peralta, A., Rao, P., 2022, Monitoring and prediction of porosity in laser powder bed fusion using physics-informed meltpool signatures and machine learning. Journal of Materials Processing Technology:117550.
- [8] Yang, L., Lo, L., Ding, S., Özel, T., 2020, Monitoring and detection of meltpool and spatter regions in laser powder bed fusion of super alloy inconel 625. Progress in Additive Manufacturing, 5:367–378.
- [9] Francois, M.M., Sun, A., King, W.E., Henson, N.J., Tourret, D., Bronkhorst, C.A., Carlson, N.N., Newman, C.K., Haut, T., Bakosi, J., et al., 2017, Modeling of additive manufacturing processes for metals: Challenges and opportunities. Current Opinion in Solid State and Materials Science, 21:198–206.
- [10] Repossini, G., Laguzza, V., Grasso, M., Colosimo, B.M., 2017, On the use of spatter signature for in-situ monitoring of laser powder bed fusion. Additive Manufacturing, 16:35–48.

- [11] Lane, B., Whitenton, E., Moylan, S., 2016. Multiple sensor detection of process phenomena in laser powder bed fusion. In: Proceedings of the Thermosense: Thermal Infrared Applications XXXVIII, Volume 9861, International Society for Optics and Photonics. 986104.
- [12] Remani, A., Williams, R., Thompson, A., Dardis, J., Jones, N., Hooper, P., Leach, R., 2021. Design of a multi-sensor measurement system for in-situ defect identification in metal additive manufacturing. In: Proceedings of the ASPE/euspen Advancing Precision in Additive Manufacturing.
- [13] Heigel, J.C., Lane, B., Levine, L., Phan, T., Whiting, J., 2020, In situ thermography of the metal bridge structures fabricated for the 2018 additive manufacturing benchmark test series. Journal of Research of the National Institute of Standards and Technology, 125.
- [14] Lough, C.S., Wang, X., Smith, C.C., Landers, R.G., Bristow, D.A., Drallmeier, J.A., Brown, B., Kinzel, E.C., 2020, Correlation of swir imaging with lpbf 304l stainless steel part properties. Additive Manufacturing, 35:101359.
- [15] Hooper, P.A., 2018, Melt pool temperature and cooling rates in laser powder bed fusion. Additive Manufacturing, 22:548–559.
- [16] Mitchell, J.A., Ivanoff, T.A., Dagel, D., Madison, J.D., Jared, B., 2020, Linking pyrometry to porosity in additively manufactured metals. Additive Manufacturing, 31:100946.
- [17] Bisht, M., Ray, N., Verbist, F., Coeck, S., 2018, Correlation of selective laser melting-melt pool events with the tensile properties of ti-6al-4v eli processed by laser powder bed fusion. Additive Manufacturing, 22:302–306.
- [18] Chen, R., Imani, M., Imani, F., 2021, Joint active search and neuromorphic computing for efficient data exploitation and monitoring in additive manufacturing. Journal of Manufacturing Processes, 71:743–752.
- [19] Yavari, R., Riensche, A., Tekerek, E., Jacquemetton, L., Halliday, H., Vandever, M., Tenequer, A., Perumal, V., Kontsos, A., Smoqi, Z., et al., 2021, Digitally twinned additive manufacturing: Detecting flaws in laser powder bed fusion by combining thermal simulations with in-situ meltpool sensor data. Materials & Design, 211:110167.
- [20] Pakkenberg, B., Pelvig, D., Marner, L., Bundgaard, M.J., Gundersen, H.J.G., Nyengaard, J.R., Regeur, L., 2003, Aging and the human neocortex. Experimental Gerontology, 38:95–99.
- [21] Everton, S.K., Hirsch, M., Stravroulakis, P., Leach, R.K., Clare, A.T., 2016, Review of in-situ process monitoring and in-situ metrology for metal additive manufacturing. Materials & Design, 95:431–445.
- [22] Wang, C., Tan, X., Tor, S., Lim, C., 2020, Machine learning in additive manufacturing: State-of-the-art and perspectives. Additive Manufacturing: 101538.
- [23] Colosimo, B.M., Grasso, M., 2020, In-situ monitoring in I-pbf: opportunities and challenges, Procedia CIRP, 94:388–391.
- [24] Gaikwad, A., Imani, F., Rao, P., Yang, H., Reutzel, E., 2019. Design rules and in-situ quality monitoring of thin-wall features made using laser powder bed fusion. In: Proceedings of the ASME 14th International Manufacturing Science and Engineering Conference, American Society of Mechanical Engineers Digital Collection.
- [25] Imani, F., Chen, R., Diewald, E., Reutzel, E., Yang, H., 2019, Deep learning of variant geometry in layerwise imaging profiles for additive manufacturing quality control. Journal of Manufacturing Science and Engineering, 141:111001.
- [26] Chen, R., Imani, F., Reutzel, E., Yang, H., 2018, From design complexity to build quality in additive manufacturing-a sensor-based perspective. IEEE Sensors Letters. 3:1–4.
- [27] Yazdi, R.M., Imani, F., Yang, H., 2020, A hybrid deep learning model of processbuild interactions in additive manufacturing. Journal of Manufacturing Systems, 57:460–468.
- [28] Song, L., Bagavath-Singh, V., Dutta, B., Mazumder, J., 2012, Control of melt pool temperature and deposition height during direct metal deposition process. The International Journal of Advanced Manufacturing Technology, 58:247–256.
- [29] Craeghs, T., Bechmann, F., Berumen, S., Kruth, J.-P., 2010, Feedback control of layerwise laser melting using optical sensors. Physics Procedia, 5:505–514.
- [30] Yadroitsev, I., Krakhmalev, P., Yadroitsava, I., 2014, Selective laser melting of ti6al4v alloy for biomedical applications: Temperature monitoring and microstructural evolution. Journal of Alloys and Compounds, 583:404–409.
- [31] Alberts, D., Schwarze, D., Witt, G., 2017. In situ melt pool monitoring and the correlation to part density of inconel 718 for quality assurance in selective laser melting. In: Proceedings of the 28th Annual International Solid Freeform Fabrication Symposium, Austin, TX, USA, pp. 7–9.
- [32] Nadipalli, V.K., Andersen, S.A., Nielsen, J.S., Pedersen, D.B., 2019. Considerations for Interpreting In-situ Photodiode Sensor Data in Pulsed Mode Laser Powder Bed Fusion.
- [33] Montazeri, M., Yavari, R., Rao, P., Boulware, P., 2018, In-process monitoring of material cross-contamination defects in laser powder bed fusion. Journal of Manufacturing Science and Engineering, 140:111001.
- [34] Taherkhani, K., Sheydaeian, E., Eischer, C., Otto, M., Toyserkani, E., 2021, Development of a defect-detection platform using photodiode signals collected from the melt pool of laser powder-bed fusion. Additive Manufacturing, 46:102152.
- [35] Grasso, M., Colosimo, B.M., 2017, Process defects and in situ monitoring methods in metal powder bed fusion: a review. Measurement Science and Technology, 28:044005.
- [36] Okaro, I.A., Jayasinghe, S., Sutcliffe, C., Black, K., Paoletti, P., Green, P.L., 2018. Automatic Fault Detection for Selective Laser Melting Using Semi-supervised Machine Learning.
- [37] Jayasinghe, S., Paoletti, P., Sutcliffe, C., Dardis, J., Jones, N., Green, P.L., 2021, Automatic quality assessments of laser powder bed fusion builds from photodiode sensor measurements. Progress in Additive Manufacturing, 1–18.

- [38] Imani, M., Saikishan, P., Saransh, G., Minxuan, Z., Yeseong, K., Tajana, R., 2020. Dual: acceleration of clustering algorithms using digital-based processing inmemory. In: Proceedings of the 53rd Annual IEEE/ACM International Symposium on Microarchitecture (MICRO), Volume 1, IEEE Computer Society, pp. 356–371.
- [39] Kanerva, P., 2009, Hyperdimensional computing: An introduction to computing in distributed representation with high-dimensional random vectors. Cognitive Computation, 1:139–159.
- [40] Kleyko, D., Osipov, E., 2014. Brain-like classifier of temporal patterns. In: Proceedings of the International Conference on Computer and Information Sciences (ICCOINS), IEEE, pp. 1–6.
- [41] Moin, A., Zhou, A., Rahimi, A., Menon, A., Benatti, S., Alexandrov, G., Tamakloe, S., Ting, J., Yamamoto, N., Khan, Y., et al., 2021, A wearable biosensing system with in-sensor adaptive machine learning for hand gesture recognition. Nature Electronics, 4:54–63.
- [42] Imani, M., Kim, Y., Riazi, S., Messerly, J., Liu, P., Koushanfar, F., Rosing, T., 2019. A framework for collaborative learning in secure high-dimensional space. In: Proceedings of the IEEE 12th International Conference on Cloud Computing (CLOUD), IEEE, pp. 435–446.
- [43] Zou, Z., Alimohamadi, H., Zakeri, A., Imani, F., Kim, Y., Najafi, M.H., Imani, M., 2022, Memory-inspired spiking hyperdimensional network for robust online learning. Scientific Reports, 12:1–13.
- [44] Kanerva, P., 1998. Encoding structure in boolean space. In: Proceedings of the ICANN 98. Springer, pp. 387–392.

- [45] Zou, Z., Kim, Y., Imani, F., Alimohamadi, H., Cammarota, R., Imani, M., 2021. Scalable edge-based hyperdimensional learning system with brain-like neural adaptation. In: Proceedings of the International Conference for High Performance Computing, Networking, Storage and Analysis, pp. 1–15.
- [46] Imani, M., Messerly, J., Wu, F., Pi, W., Rosing, T., 2019. A binary learning framework for hyperdimensional computing. In: Proceedings of the Design, Automation & Test in Europe Conference & Exhibition (DATE), IEEE, pp. 126–131.
- [47] Politecnico di milano. (www.polimi.it) (Accessed 2021).
- [48] Trumpf. (www.trumpf.com) (Accessed 2021).
- [49] Gronle, M., Grasso, M., Granito, E., Schaal, F., Colosimo, B.M., 2022, Open data for open science in industry 4.0: In-situ monitoring of quality in additive manufacturing. Journal of Quality Technology, 1–13.
- [50] Wong, K.V., Hernandez, A., 2012, A review of additive manufacturing. International Scholarly Research Notices, 2012.
- [51] Cortes, C., Vapnik, V., 1995, Support-vector networks. Machine Learning, 20:273–297.
- [52] Fix, E., Hodges, J.L., 1989, Discriminatory analysis. nonparametric discrimination: Consistency properties. International Statistical Review/Revue Internationale Délelőtt Statistique, 57:238–247.
- [53] Cohen, P., West, S.G., Aiken, L.S., 2014, Applied Multiple Regression/Correlation Analysis for the Behavioral Sciences. Psychology Press.
- [54] Cover, T.M., 1965, Geometrical and statistical properties of systems of linear inequalities with applications in pattern recognition. IEEE Transactions on Electronic Computers, 326–334.